PREPARED FOR SUBMISSION TO JINST

The Thomson scattering diagnostic at Wendelstein 7-X and its performance in the first operation phase.

S.A. Bozhenkov, [a,1] **M. Beurskens,**[a] **A. Dal Molin,**[b] **G. Fuchert,**[a] **E. Pasch,**[a] **M.R. Stoneking,**[c] **M. Hirsch,**[a] **U. Höfel,**[a] **J. Knauer,**[a] **J. Svensson,**[a] **H. Trimino Mora,**[a] **R.C. Wolf**[a] **and W7-X team**

[a] *Max-Planck-Institut für Plasmaphysik, D-17491 Greifswald, Germany*
[b] *Università degli Studi di Milano-Bicocca, Milan, Italy*
[c] *Lawrence University, Appleton, Wisconsin, USA*

E-mail: `sergey.bozhenkov@ipp.mpg.de`

ABSTRACT: The optimized stellarator Wendelstein 7-X started operation in December 2015 with a 10 week limiter campaign. Divertor experiments will begin in the second half of 2017. The W7-X Thomson scattering system is an essential diagnostic for electron density and temperature profiles. In this paper the Thomson scattering diagnostic is described in detail, including its design, calibration, data evaluation and first experimental results. Plans for further development are also presented.

The W7-X Thomson system is a Nd:YAG setup with up to five lasers, two sets of light collection lenses viewing the entire plasma cross-section, fiber bundles and filter based polychromators. To reduce hardware costs, two or three scattering volumes are measured with a single polychromator. The relative spectral calibration is carried out with the aid of a broadband supercontinuum light source. The absolute calibration is performed by observing Raman scattering in nitrogen. The electron temperatures and densities are recovered by Bayesian modelling. In the first campaign, the diagnostic was equipped for 10 scattering volumes. It provided temperature profiles comparable to those measured using an electron cyclotron emission diagnostic and line integrated densities within 10% of those from a dispersion interferometer.

KEYWORDS: Plasma diagnostics

---

[1] Corresponding author.

Contents

1 Introduction

Wendelstein 7-X (W7-X) is a large optimized stellarator with superconducting coils [1, 2]. The optimization includes low neoclassical transport, high equilibrium β, good MHD properties, small bootstrap current and improved fast-ion confinement. The aim of the project is to demonstrate the viability of the stellarator line as a fusion reactor concept [3]. The optimization procedure is detailed in [4] and a historical perspective is presented in [5].

W7-X operation started with a limiter campaign, named OP1.1, that lasted from December 2015 until March 2016. Five graphite inboard limiters defined the plasma boundary [6] and only discharges with electron cyclotron resonance heating (ECRH) with total injected energy below 4 MJ were performed. The campaign was devoted to an integral machine commissioning, but some promising physics results were achieved as well. Plasmas with electron temperature up to 7 keV, ion temperature up to 2 keV and electron densities up to $3 \cdot 10^{19}$ m^{-3} in the flat-top phases were realized [7, 8].

To achieve steady-state operation with ECRH heating up to 10 MW, W7-X will be equipped with an island divertor [9, 10]. First, in the campaign OP1.2 planned for the second half of 2017, inertially cooled graphite divertor targets will be used to establish divertor operation and to explore the operational space. For later campaigns (OP2), water-cooled graphite divertor targets of the same shape will be installed with the aim of realizing up to 30 minute long discharges [11]. The W7-X campaigns and the corresponding machine capabilities are detailed in [3].

Good diagnostic coverage is essential for physics studies at W7-X. In particular, profile information for electron temperature and density is necessary, for example, for confinement and transport studies [12, 13], for investigations of profile resilience with ECRH deposition [8], and is also an important input for numerical codes. At W7-X the Thomson scattering system is a standard profile diagnostic for electron temperature and density. In this paper, the W7-X Thomson scattering diagnostic is described in detail.

Incoherent Thomson scattering is a well established experimental technique [14], which is successfully applied on many fusion devices [15–19]. Powerful lasers are routinely used for Thomson scattering to achieve acceptable signal to noise ratios. The differential scattered power P_s can be generally written as follows:

$$\frac{d^3 P_s}{d\epsilon d\Omega dV} = r_e^2 n_e \langle S_\ell \rangle S(\epsilon, \theta, \alpha), \tag{1.1}$$

where r_e is the classical electron radius, S_ℓ is Poynting vector of the incident laser light, θ is scattering angle, $\epsilon \equiv (\lambda - \lambda_\ell)/\lambda_\ell$ is normalized wavelength shift and α is normalized inverse temperature $m_e c^2/(2T_e)$. The spectral density function $S(\epsilon, \theta, \alpha)$ contains information about electron temperature and can be calculated by taking an integral over the electron distribution [14]. An analytic approximation of the spectral density function was given by Naito [20, 21] for the most common measurement configuration, where both the incident and the observed light is polarized perpendicular to the scattering plane.

In order to maintain an acceptable signal to noise ratio, the scattered spectrum is usually measured only in a few spectral intervals. Such a polychromator system is realized by a set of interference filters and avalanche photodiodes. The output value of interest for each channel is the time integral of the signal s over the length of the scattered laser pulse. It corresponds to the number of the scattered photons and can be approximated for a polychromator channel i as:

$$\left(\int s dt\right)_i = n_e E_\ell \frac{r_e^2}{hc} \cdot \delta\Omega g_0 \cdot \int\int S(\epsilon, \theta, \alpha) \cdot \frac{\lambda}{\lambda_\ell} \cdot \frac{g_i(\lambda)}{g_0} \cdot dL d\lambda, \tag{1.2}$$

where the time integration is over the laser pulse. E_ℓ is the laser pulse energy, $\delta\Omega$ is the solid angle of the light collection optics, $g_i(\lambda)$ is the absolute sensitivity of the ith polychromator channel including the filter transmission and electronic gains, $g_0 \equiv g_r(\lambda_r)$ is the absolute sensitivity of a reference channel at a reference wavelength. The sensitivity value g_0 is by definition unique for every polychromator. The integration on the right hand side is over the wavelength and over the length of the observation volume along the laser line. If the plasma parameters do not change significantly in the observation volume the latter integration reduces to multiplication by the volume length δL.

Practical applications of Thomson scattering require careful system calibration. Since it is often not possible to absolutely calibrate all spectral channels, the calibration is usually split into two stages. The spectral calibration of the channel sensitivities relative to a selected reference channel $g(\lambda)/g_0$, where the reference wavelength is chosen rather arbitrarily, can be performed independently from the absolute sensitivity calibration. The latter measures in situ the factor $\delta L \delta\Omega g_0$ using either Rayleigh or Raman scattering of light from the same laser as used for plasma measurements.

The W7-X incoherent Thomson scattering system is a Nd:YAG setup using polychromators for spectral analysis. Its hardware installation was previously described in [22]. In this paper we introduce only essential parts of the diagnostic, discuss its spatial resolution, spectral and absolute calibration procedures, data evaluation and compare measurement results from the first W7-X campaign with data from the electron cyclotron emission diagnostic (ECE) and from the dispersion interferometer. We also present plans for the further development of the Thomson system.

The relative spectral calibration of the W7-X system is carried out using a pulsed supercontinuum light source and a scanning monochromator. The procedure simultaneously includes all parts of the system with exception of the vacuum window. The absolute in situ calibration is performed with Raman scattering in nitrogen observed in two spectral channels. Plasma electron temperatures and densities are recovered by Bayesian modelling using the Minerva framework [23]. In this paper, a Bayesian forward model for Thomson scattering is developed and different possible types of the posterior distribution are discussed.

The W7-X Thomson scattering system was operational from the first day of the campaign OP1.1 with 10 scattering volumes on the outboard half of the plasma cross-section and with a single Nd:YAG laser at 10 Hz. The temperature profiles obtained from the Thomson scattering were in general consistent with those measured with the W7-X ECE diagnostic. Also density profiles measured with the Thomson scattering were in a good agreement with the line integrated values from the interferometry. The Thomson system will be upgraded for future experiments both in spatial and in temporal resolution.

The rest of the paper is organized in the following way: first in section 2 the hardware setup of the W7-X Thomson scattering is described; then in sections 3 and 4 details of the spectral and absolute calibrations are covered; in section 5 the data processing and Minerva modelling are explained and numerical studies of the system capabilities are presented; in section 6 experimental results from the first W7-X campaign are shown; and finally in section 7 the results of the paper are summarized.

2 The W7-X Thomson scattering system

The W7-X Thomson scattering diagnostic is a Nd:YAG system. An overview of the setup is shown schematically in figure 1. The laser light, $\lambda = 1064$ nm, is guided through the plasma roughly horizontally and passes close to the magnetic axis, making direct measurements of the Shafranov shift possible. The laser light is dumped outside of the vacuum vessel. The light scattered by plasma is collected with two front optics into a set of fiber bundles, each fiber bundle defining a scattering volume. The fiber bundles transfer the light to polychromators, where the spectral analysis and the light detection is performed. The signals are digitized, stored in the experimental archive, and are used to reconstruct both the electron temperature and the electron density.

The system is designed for operation with up to five Nd:YAG lasers, that can be triggered either simultaneously to increase the pulse energy or with delays to increase the time resolution. For easy access and maintenance, the lasers are located in a dedicated laser room outside of the experimental hall. The laser light is delivered to the plasma vessel via a carefully designed 30 m long system of dielectric mirrors. The laser pulse energy ranges from 0.7 to 2.4 J; the pulse length is about 10 ns; the repetition rate of each laser is 10 Hz; and the input beam is linearly polarized perpendicular to the scattering plane. In the first campaign OP1.1, only one laser was operated, i.e. the time resolution was limited to 100 ms. In the next campaign OP1.2, three lasers will be available resulting in an increased sampling frequency up to 30 Hz. In addition a burst mode with short pulse trains of up to 10 kHz is planned.

After leaving the vessel, the laser light is directed to a laser energy monitor and a beam dump, which are both about 3 m beyond the output port. The input and output vacuum windows are located at

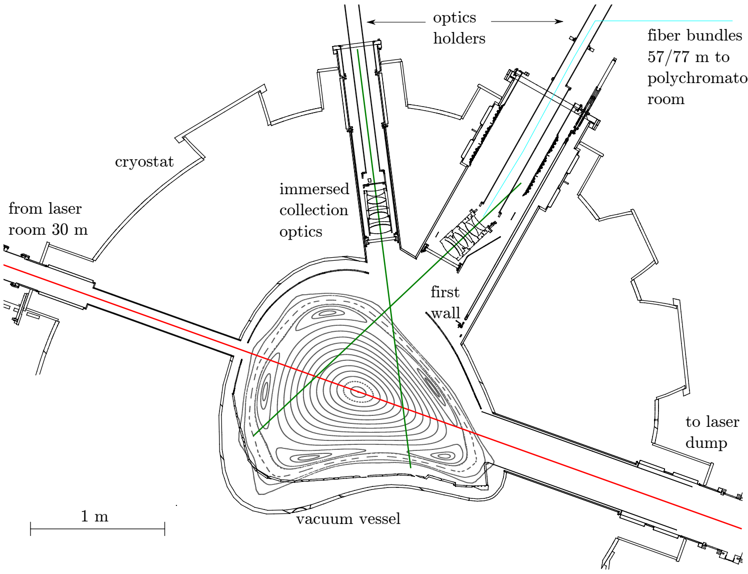

Figure 1. W7-X Thomson scattering setup. The laser light enters the vessel from the inboard side of the machine, passes through the plasma center, and leaves the vessel at the outboard side. The full plasma cross-section is observed with two sets of optics. The scattered light is transferred with fiber bundles to a polychromator room.

the ends of the port tubes. These system features minimize the disturbance of the measurements by the stray laser light. The spectral filters in the polychromators provide an additional suppression of stray light.

The full plasma cross-section of about 1.6 m is observed with two sets of optics specially designed for the wavelength range from 700 to 1064 nm [24]. Each optics set observes one half of the cross-section, and therefore they can be referred to as inboard and outboard. The main parameters of the optics are: the focal length is 172 mm; the distance to the laser beam path is about 1.3 m; the diameter of the outboard optics 160 mm; the dimensions of the inboard optics are 90 × 160 mm; the typical solid angle is about 8 msr; both systems are designed for fibers with numerical aperture up to 0.37; the optical demagnification varies between 7 and 11. The optics sets are mounted on retractable manipulators and during measurements are placed inside the ports on the air side of the vacuum windows. The optics are retracted to readjust or replace fiber bundles, and for protection during baking of the machine. The re-insertion of the optics is precise to about 0.1 mm.

The laser mirrors and the optics sets are mounted on a special structure called Thomson bridge [22]. The Thomson bridge is mechanically decoupled from the vacuum and cryostat vessels, thus ensuring optical stability. Indeed, the experiments in OP1.1 showed that the system remains adjusted and performs well during an experimental day. Losses of the adjustment happened only between experimental days, when general access to the bridge was open. It is worth mentioning that the bridge also serves as an access to the inner part of the torus. The system operation was guaranteed by an inspection and a fine adjustment of the laser to the calibration marks at the windows before an experimental day. Such readjustments can lead to additional errors in measured density, as discussed later in the paper. An automated adjustment with monitoring cameras and remotely-steerable mirrors is under development.

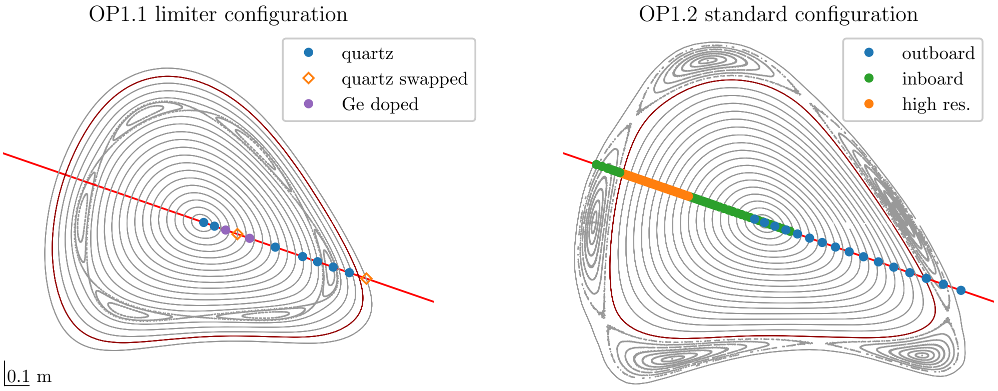

Figure 2. Scattering volumes in the OP1.1 campaign limiter configuration (left) and standard divertor configuration of OP1.2 campaign (right). In OP1.1 the outboard side was covered with 10 volumes, two of the volumes were observed with Ge-doped fibers. One of the fibers was moved in the middle of the campaign from the edge to the core. In the next campaign, OP1.2, the outboard side will be extended to 16 volumes, and the inboard side will be covered with 79 volumes. In both cases the last closed flux surface (LCFS) is indicated.

The scattered light is collected into fiber bundles, transferring it to polychromators for spectral analysis. The arrangement of the fibers in the imaging plane defines the number of the observed scattering volumes and the spatial resolution, as illustrated in figure 2. In the first campaign, only the outboard part of the system was operated with 10 fiber bundles of rectangular cross-section 3.2×1.1 mm^2 (left part of figure 2). One of the channels was initially placed into the scrape-off layer and showed a reliable signal, but later was relocated to the core region for a better core coverage and a better comparison between channels.

Two types of optical fibers were tested: eight of the bundles have quartz cores and a numerical aperture of 0.29; two bundles have Ge-doped cores and a numerical aperture of 0.37. The packing of the Ge-doped fibers to the bundles was found to be sparser. Because of this, they do not demonstrate the expected gain in the signal quality. In addition, the high numerical aperture fibers appear to be more sensitive to the calibration conditions, as shown later in the paper. For these reasons and due to a lower price, the quartz core fibers will be used for the rest of the system.

The profile coverage will be improved for future experiments, as shown in the right part of figure 2. The outboard side will be augmented with six fiber bundles of the same size as the original ten. This upgrade is possible without modifying any mechanical components by filling available slots in the fiber holder. The inboard part of the profile will be covered with up to 79 volumes in several steps. Here fiber bundles of different cross-section width will be densely packed side by side. In the outer part of the plasma, where large gradients may occur, the inboard system will eventually have spatial resolution of about 6 mm in effective radius (highlighted with orange in figure 2). In the center the inboard and outboard optical coverage overlaps by about 15 cm, providing a self-consistency check.

The spatial resolution of the system is defined as the distance between the centers of two adjacent scattering volumes, where the volumes are optical projections of the fiber bundle cross-sections to the laser line. The arrangement of the fibers in the imaging plane dominates over the other sources.

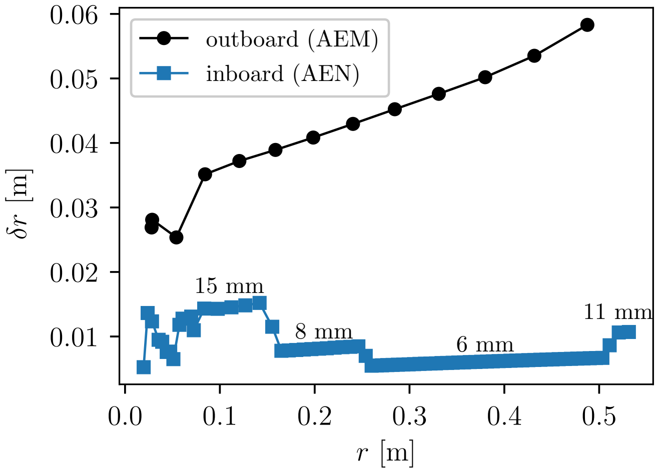

Figure 3. Resolution of the Thomson scattering system for the standard divertor configuration of campaing OP1.2. The resolution is defined as the distance between the centers of two neighbouring volumes. The distance is measured as effective radius, where the LCFS radius is about 0.5 m. The inboard and outboard sides are shown separately. The inboard side consists of regions with different resolution. The abrupt change of the resolution in the center is a numerical effect due to a small size of the flux surfaces.

The resolution measured in effective radius is presented in figure 3 for both parts of the system. The value for the outboard side changes from about 3 cm in the center to about 6 cm at the edge. For the inboard side, the areas with different resolution are defined by chosen widths of fiber bundle cross-sections: in the core the resolution is 15 mm or 8 mm; in the high resolution area it is 6 mm; in the island region the resolution is about 11 mm. The shown values are calculated for the standard W7-X divertor configuration, but the changes with magnetic configuration are small.

The high resolution inboard part of the system can be expected to be sensitive to the experimental conditions. Higher laser energies and densities may be necessary for reliable measurements. The signal to noise ratio can be improved by filtering out impurity lines and using a polariser to reduce Bremsstrahlung contamination. These options are presently under investigation.

Positions of the scattering volumes are accurately measured during maintenance periods when access to the vacuum vessel is possible. A laser tracking system is used to measure positions of the adjustment laser and of the back-illuminated images of the fiber bundles in the global W7-X coordinate system. This allows to find both centers and lengths of the scattering volumes projected to the laser line. The measured 3d positions can be mapped to plasma coordinates by using e.g. plasma equilibrium code VMEC [25] self-consistently, i.e. using experimental profiles for the equilibrium reconstruction.

The fiber bundles transfer the scattered light to polychromators for spectral analysis. To save hardware costs, some fiber bundles are merged to a single polychromator, with each additional bundle having a delay loop of 20 m to separate the signals in time. In campaign OP1.1 all fiber bundles were paired, with one end being 57 m long and the other of 77 m. Such an approach proved to be reliable and to result in a tolerable increase in the noise level. The additional noise arises because of integrating the background plasma emission from the doubled volume. The fiber bundles for the inboard side will be also combined: in the high resolution region, where signal to noise ratio is particularly important, two volumes will be sent to each polychromator and in the core three volumes will be combined per polychromator.

The spectral analysis of the scattered light is performed with filter based polychromators. The preliminary arrangement of W7-X polychromators was discussed in [26]. The optical design is for numerical aperture of 0.37 and fiber bundles with diameter of 3 mm. Five spectral channels are used to diagnose electron temperatures from about 10 eV up to about 10 keV: 750–920 nm, 920–1000 nm, 1000–1035 nm, 1035–1051 nm and 1051–1061 nm. For higher temperatures six channel polychromators will be introduced in future, as discussed later in the paper. No additional Rayleigh scattering channel is available in the W7-X setup. The optical signals are detected with temperature stabilized avalanche photodiodes.

The photodiode outputs are AC filtered to remove the constant background, amplified and digitized with a sampling rate of 1 GS/s and 14 bit resolution (SP Devices ADQ-14). The acquisition system records time resolved laser pulses, which helps to identify reflection events and improves the signal to noise ratio. The digitized signals are used in the post-analysis to recover both the most likely temperature and density.

It should be noted that presently the system is operated without a polariser in the collection optics, which is required for a strict application of Naito's approximation to the spectral density function (equation 1.1). Numerical integration of the full expression demonstrates that the associated correction for the present experimental conditions is at a negligible level of less than 1% for the density measurement and even smaller for the temperature. A polariser also improves the signal to noise ratio and therefore is considered for installation in future. The installation is possible either in front of the collection optics or in front of the fiber bundles. In the first case the polariser must be 160 mm in diameter and must withstand temperatures up to 200 °C. In the latter case the requirements to the polariser are relaxed, but Faraday rotation up to 50° in the optics, about 30 cm of glass in about 1 T field, has to be accounted for. The Faraday rotation changes with the machine magnetic configuration, wavelength and scattering volume. For this reason this option is presently less favoured.

3 Spectral calibration

The relative spectral calibration provides factors $g(\lambda)/g_0$ for all spectral channels of all scattering volumes, see equation 1.2. The procedure at W7-X simultaneously calibrates the front optics, the fiber bundles, the polychromators and the electronics. The vacuum window transmission coefficient is measured and taken into account separately. Possible vignetting by the in-vessel structures and equivalence of the light cone are presently not accounted for as it requires an in-vessel calibration. This can lead to systematic errors in the plasma measurements, because the ratio of channel sensitivities can change with the angular distribution of light. An example of plasma measurements where this is suspected to be the case is given later in the paper.

A sketch of the spectral calibration setup is shown in figure 4a. A supercontinuum light source (Super-K compact by NKT Photonics) generates about 2 ns long pulses covering a wide spectrum with repetition rate of 30 kHz. A monochromator (Spex 750M) is used to select a narrow wave-

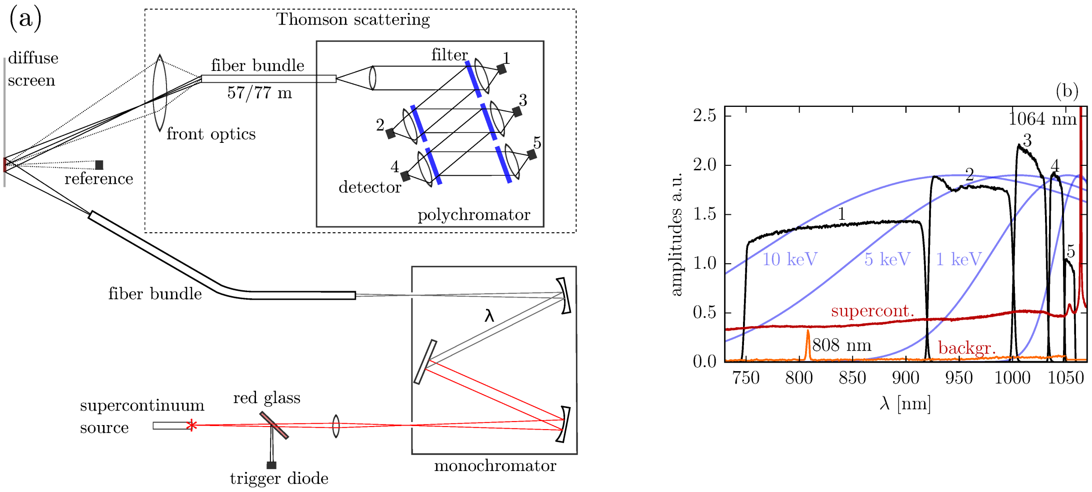

Figure 4. Spectral calibration. (a) - spectral calibration setup. A narrow wavelength range is selected from the output of a supercontinuum source with a monochromator. The single wavelength is used to illuminate a diffuse screen in front of the optics. (b) - typical calibration results. In the figure also Thomson scattering spectra for temperatures of 0.1, 1, 5 and 10 keV, the supercontinuum spectrum (“supercont.”) and the CW background of the supercontinuum source (“backgr.”) obtained with long integration time are given. The pronounced spectral lines are: Nd:YAG at 1064 nm and CW pump diode at 808 nm.

length interval for a measurement. The monochromator output is delivered with a fiber bundle to the stellarator hall. During spectral calibration the front optics with the mounted fibers is retracted from the port and a spectrally neutral diffuse screen is placed in front of it. This screen is illuminated with the fiber bundle from the monochromator. In a calibration run the monochromator wavelength is scanned over the range of interest, and the intensity reflected by the diffuse screen is monitored with a reference photodiode.

In the calibration setup the angular distribution of the intensity is not necessarily equivalent to that during plasma measurements. In both cases the light collection is limited by the numerical aperture of the fibers. But in the calibration case the light source, i.e. the screen, is placed much closer to the optical system, which implies that to reproduce the plasma case also a spatial uniformity of the spot is required. This is approximated by illuminating an oversized area. Possible systematic influence of this approach will be investigated in future.

A typical spectral calibration measurement for five spectral channels is illustrated in figure 4b. Each curve was measured with a wavelength step of 0.1 nm and for each wavelength 200 pulses were accumulated for statistics. The difference in the magnitude of the response between channels 4 and 5 is mainly due to the setting of the APD voltage. The supercontinuum spectrum detected with the reference diode can also be found in the figure. The source spectrum is rather flat in the region covered by filters; outside of this region the Nd:YAG wavelength of 1064 nm can be seen. This line can be used to estimate the spectral resolution of the measurement and together with an additional CW line of the pump diode at 808 nm to calibrate the wavelength scale. The spectral resolution estimated as the FWHM of the Nd:YAG line is about 0.4 nm.

4 Absolute calibration

Absolute calibration of the W7-X Thomson scattering system is performed using anti-Stokes rotational Raman scattering in nitrogen, as first proposed in [27] and now used at several fusion experiments [28, 29]. This method does not require an additional spectral channel at the laser wavelength and is not sensitive to laser stray light. The anti-Stokes part of the rotational Raman spectrum consists of multiple narrow lines due to $J \to J-2$ transitions, where J is the rotational quantum number. The integrated signal detected by a spectral channel for a laser pulse is found by summing all the lines (compare to equation 1.2):

$$\left(\int s\,dt\right)_i = n_{N2}E_0\cdot\sum_J \frac{d\sigma_J}{d\Omega} f_J \frac{\lambda_J}{hc}\frac{g_J}{g_0}\cdot\delta L\delta\Omega g_0 \equiv n_{N2}E_0 R\cdot\delta L\delta\Omega g_0 \tag{4.1}$$

Here n_{N2} is the nitrogen particle density, E_0 is the laser pulse energy, $\frac{d\sigma_J}{d\Omega}$ is the differential cross-section for the line λ_J, f_J is the fractional population of the upper state, $g_J/g_0 \equiv g_i(\lambda_J)/g_0$ is the relative sensitivity of the system at the wavelength and R is a brief notation aggregating known values. The product of the scattering volume length δL, solid angle $\delta\Omega$ and the channel sensitivity g_0 including the transmission losses and the reference photodiode gain can be found from linear scaling with gas pressure, given the relative spectral calibration and the molecular constants. The differential cross-section is [30, 31]:

$$\frac{d\sigma_J}{d\Omega} = \frac{64\pi^4}{45}\frac{3J(J-1)}{2(2J+1)(2J-1)}\frac{\gamma^2}{\lambda_J^4}\cdot F, \tag{4.2}$$

where F is a factor depending on the scattering geometry and observed polarization. For the case without a polarizer considered here the value of F is 7/4. The value of the anisotropy of the polarizability tensor γ^2 has a weak dependence on the wavelength and was measured to be

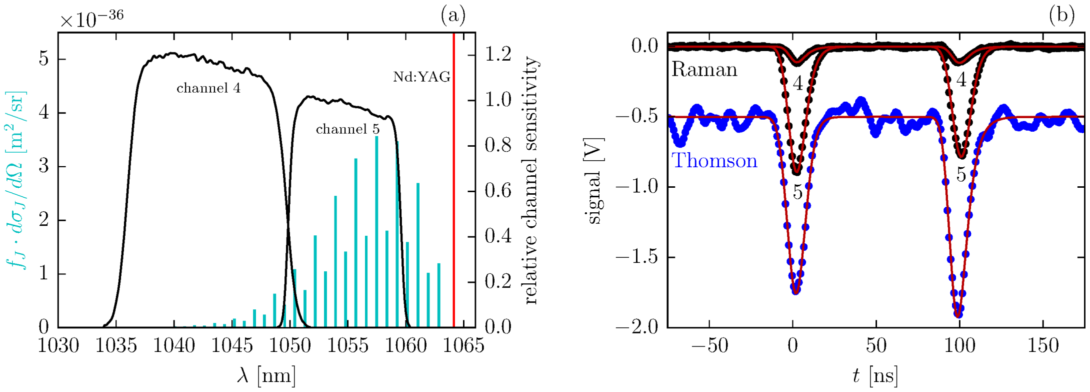

Figure 5. Raman scattering calibration. (a) - anti-Stokes rotational Raman lines in nitrogen. Effective cross sections of the lines including the relative level populations are overlaid with typical spectral curves of two Thomson channels. (b) - typical Raman scattered signals for the spectral channels 4 and 5 at nitrogen pressure of about 100 mbar and laser pulse energy of 1 J. For comparison a Thomson scattering signal from the spectral channel 1 from plasma with T_e of about 6 keV and n_e of about $1.3\cdot 10^{19}$ m^{-3} and laser pulse energy of 1.5 J is shown with an offset of -0.5 V.

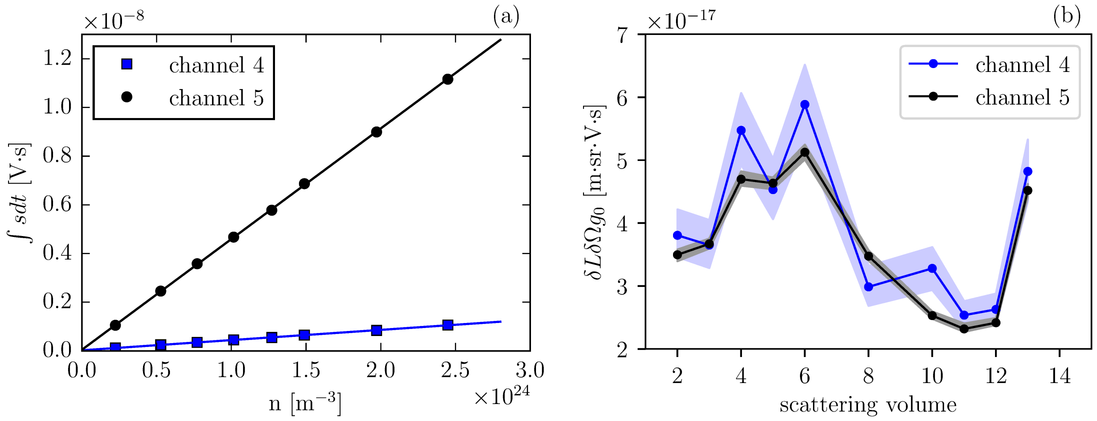

Figure 6. Results of the Raman scattering calibration. (a)- measured signals for spectral channels 4 and 5 versus nitrogen density. The solid lines are linear fits to the experimental data: $k_4 \approx 4.20 \pm 0.04 \times 10^{-34}$, $k_5 \approx 4.55 \pm 0.02 \times 10^{-33}$. Each data point is averaged over 500 laser pulses. (b) - calibration factor $\delta L \delta \Omega g_0$ for the ten scattering volumes as found from the Raman calibration. The colored areas show the sensitivity to a wavelength shift of ±0.25 nm for the spectral calibration.

$(5.1 \pm 0.25) \times 10^{61}$ m^6 for the Nd:YAG wavelength [28]. The relative level population is given by the Boltzmann distribution:

$$f_J = \frac{w_J(2J+1)}{Z} \exp\left(-E_J/kT\right), \tag{4.3}$$

w_J is a statistical weight, which for nitrogen is 3 for odd values of J and is 6 for even values [30]. The normalization constant Z is chosen such that $\sum_J f_J = 1$. The rotational level energy is $E_J = hc(B_0 J(J+1) - D_0 J^2 (J+1)^2)$, with molecular constants $B_0 = 1.99 \cdot 10^2$ m^{-1} and $D_0 = 5.76 \cdot 10^4$ m^{-1} taken from [32]. During the measurements at W7-X the temperature of the plasma vessel is monitored with thermocouples, and the gas is assumed to be in thermal equilibrium with the walls.

Anti-Stokes rotational lines of nitrogen are illustrated in figure 5a, where the effective cross-sections, including the relative level populations for room temperature, are plotted. The lines have a significant amplitude in the range of the Thomson spectral channels 4 and 5. An example of the measured signals is given in figure 5b for nitrogen pressure of about 100 mbar and laser energy of 1 J. As expected, the amplitude of the signal in channel 5 is about an order of magnitude higher than that in channel 4. The two peaks separated by about 100 ns appear because of combining fiber bundles from two volumes with a delay loop of 20 m. For comparison an example of the Thomson scattered light from the plasma at the density of $1.3 \cdot 10^{19}$ m^{-3} and laser pulse energy of 1.5 J is also shown in the figure. The Thomson scattered signal is offset by -0.5 V for clarity. The Raman signals have a higher signal to noise ratio as compared to the Thomson scattered signal, because in the plasma case considerable Bremsstrahlung background radiation is present.

Dependence of the Raman signals in the spectral channels 4 and 5 on the nitrogen density is shown in figure 6a. Each data point in the plot is averaged over 500 laser pulses; as a consequence, the statistical errors are small. The solid lines in the figure represent the corresponding linear fits. For all scattering volumes the stray laser light is insignificant, as evidenced by the zero intercepts for the linear regressions. The slope of the lines is determined with a statistical error of about 1%.

The calibration factors $\delta L \delta \Omega g_0$ calculated from equation 4.1 for the scattering volumes used in OP1.1 are plotted in figure 6b and have a small statistical uncertainty. The dependence of the calibration factor on the scattering volume is dominated by the absolute gain settings of avalanche photodiodes in the reference channels g_0. Values obtained from the two spectral channels for one polychromator have to coincide. The factors calculated from channels 4 and 5 are indeed of the same order, but do show a noticeable difference for some volumes. This discrepancy is likely related to the details of the spectral calibration. Because in spectral channel 4 the Raman lines are located in the region of rapid variation in the filter transmission, a change in the wavelength scale of about 0.25 nm or equivalently in the incidence angle on the interference filter of 2° can bring the channel 4 results to the level of channel 5. At the same time the corresponding change in channel 5 is only about 4%. A uniform shift of the wavelength scale is not sufficient to explain the changes of the discrepancy for different scattering volumes, since it would shift the whole dependence in figure 6b. Insufficiently uniform illumination of the light cone during the spectral calibration for some volumes is more likely to be the reason.

The absolute calibration factor $\delta L \delta \Omega g_0$ can be reliably determined from the spectral channel 5 with the individual point error estimated at about 4% as caused by non ideal spectral calibration. All values have the same systematic uncertainty of 5% due to the value of the anisotropy of polarizability tensor γ in equation 4.2. The influence of the gas temperature uncertainty on the result is 1 %/K for channel 4 and 0.1%/K for channel 5; and is negligible for a typical measured change of the vessel temperature of less than 0.5 K during the entire calibration.

5 Evaluation of electron temperature and density

For each laser pulse the acquisition system records time resolved traces of the scattered radiation for all spectral channels. An example of recorded data is given in figure 5b. To reconstruct electron temperatures and densities from such time traces a two stage approach is used. First, the signals are individually fitted with a model pulse and the time integral of the pulse is calculated. Subsequently, the integrated values for all spectral channels for a volume are modelled with Bayesian approach to simultaneously determine the most likely temperature and density, and their uncertainties.

For the W7-X system, an accurate fitting of the scattered pulse is achieved with a convolution of a Gaussian laser pulse and a first order low-pass filter of the amplifier. The typical laser pulse full-width-at-half-maximum and the low pass filter time constant are about 10 ns and 3 ns correspondingly. An example of the fitting is shown with solid lines in figure 5b both for Raman and Thomson scattering. It is important to mention that the fitting also delivers the associated statistical uncertainties necessary for the following Bayesian analysis. The background plasma radiation, which is mainly Bremsstrahlung in OP1.1, adds considerably to these uncertainties.

Bayesian probability theory provides a universal approach for determining system parameters from observations. The probability density function of the parameters given the measurements, known as the posterior distribution, is expressed as [33]:

$$p(P|D) = \frac{p(D|P) \cdot p(P)}{p(D)} \tag{5.1}$$

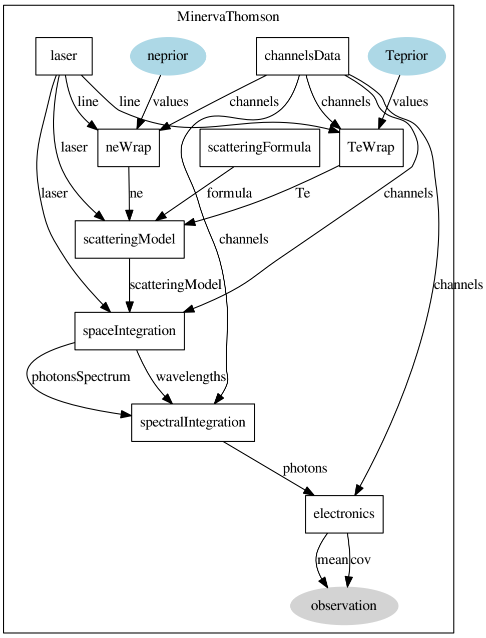

Figure 7. Minerva graph of the Thomson scattering model. Each parameter or measurement is represented by a node. The edges represent deterministic or probabilistic dependencies. Prior distributions for T_e and n_e are shown as light blue ellipses. The observation node, gray elipse, is a probabilistic node for the comparison of the forward model with the measurements.

The probability of the data given parameters $p(D|P)$, the likelihood, represents the observations, e.g. it can be a Gaussian distribution with a forward model prediction and experimental uncertainties. The prior parameter distribution $p(P)$ incorporates any previous knowledge of the problem and often can be assumed to be uniform. The evidence $p(D)$ does not influence the finding of the parameters but is rather a normalization factor, which is important for hypothesis testing.

The Bayesian approach for Thomson scattering was previously demonstrated to perform well as compared to the usual ratio method [34] and to provide asymmetries of the uncertainties and the cross-correlation between measured density and temperature [35]. The asymmetries in the uncertainties appear due to deviations of the posterior distribution from Gaussian. The cross-correlation is introduced by the measurement with a limited number of spectral channels. For example, if the scattered spectrum is so narrow that only the closest to the laser spectral channel receives signal, it becomes impossible to differentiate between the temperature and the density.

For W7-X, an independent implementation of the Thomson model in Minerva framework has been developed. Minerva [23] is a Java framework for practical applications of Bayesian analysis. It is based on graphical models, i.e. all models are graphs. Each parameter or measurement is reflected by a node of the graph and the edges between the nodes, i.e. the connections, represent deterministic or probabilistic dependencies. Minerva keeps track of the dependencies, which helps to optimize the simulations. The framework allows finding of the maximum of the posterior, sampling of the posterior with the Markov-Chain-Monte-Carlo (MCMC) method, and contains implementations of many other useful algorithms.

The graphical model of the Thomson scattering diagnostic is shown in figure 7. In this example only the electron temperature and the density are considered as unknowns. Their prior distributions, light blue ellipses in the figure, are assumed to be flat between zero and a maximal value considered plausible for a discharge. For the present work, each scattering volume is treated independently. However, with minor modifications a profile description can be implemented [36]. The forward model, the part between the priors and the observation node, is a deterministic relation between parameters and the values to be measured. This involves both space and spectral integration and scaling by the electronics. The space integration is considered explicitly to allow treatment of profiles with gradient lengths comparable with the scattering volume length, e.g. in a pedestal region. The forward model is connected to a probability observation node, shown in gray, where it is compared with measurements. The forward model and the observation node together correspond to the likelihood distribution of equation 5.1. The whole graph is a product of the prior and likelihood and, thus, is equivalent to the posterior up to an ignorable normalization.

It is straightforward to further elaborate the Thomson model e.g. by adding uncertainties of the calibration parameters or by combining it with other diagnostics. It should be noted that for such enhancements the forward model itself is not modified, but additional priors have to be connected to the parameters in question or additional graphs for other diagnostics have to be merely added. More advanced models such as these will be studied in future work.

To test the model and to verify performance of the W7-X Thomson system simulations with synthetic data were performed. Assumed values of temperature T_e and density n_e are used to first forward calculate the signals in all spectral channels and to generate synthetic measurements by addition of noise. The generated values are then inserted as observations and the Minerva framework is applied to find the most likely temperature and density, and their uncertainties. This process is known as graph inversion, which mathematically is finding maximum of the posterior distribution. The parameters of the model correspond to the W7-X system, including the calibration factors.

Gaussian distributions with fixed values of the standard deviation σ are employed to describe the noise in synthetic data, where the value of σ is a free parameter. A fixed value of σ is found to be closer to real experiment conditions than a fixed signal to noise ratio (SNR) for every spectral channel. As electron temperature changes, the signal in some spectral channels can become negligible. At the same time the background plasma light and consequently the fit uncertainty do not naturally decrease. In the case of a fixed SNR for every channel the uncertainty of such data is strongly underestimated. On the other hand, since a comparison between the noise and the signal levels is desirable, the signal to noise ratio is introduced more delicately as an average over the spectral channels.

Results of a Bayesian model are fully described by the posterior distribution. From the practical point of view, the posterior distribution around the maximum is usually of interest. Once the maximum is found, the distribution around it can be sampled with the MCMC procedure [37]. The MCMC algorithm draws random samples in such a way that their distribution converges to the posterior distribution. Here these samples and calculated posterior values for their positions are used to illustrate the posterior distribution. Because the Thomson model analyzed here depends on only two parameters, it is straightforward to illustrate such posteriors, figure 8. Each point in the figure is an MCMC sample and the colour of the point reflects its probability relative to the

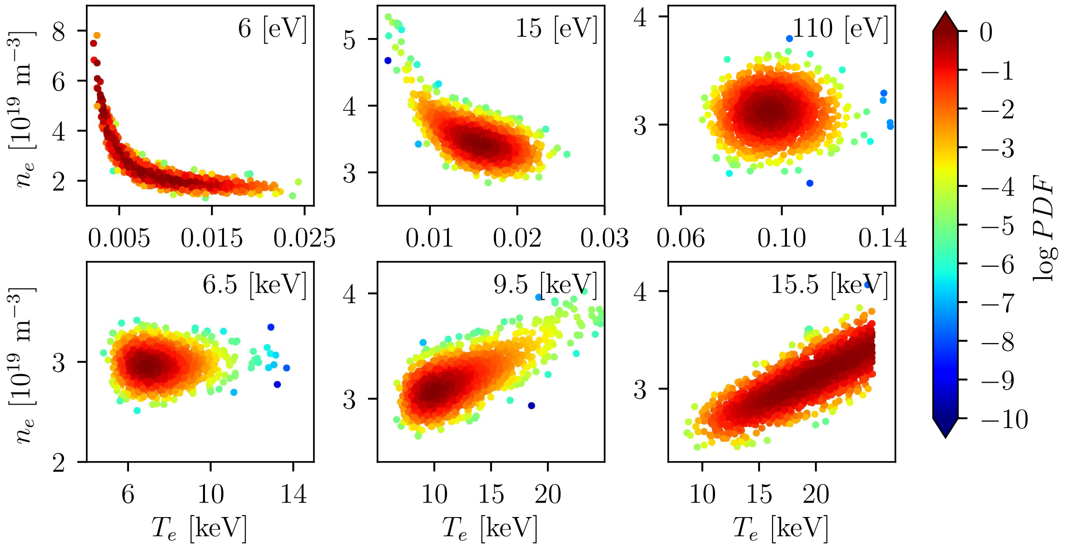

Figure 8. Posterior distributions in the temperature and density plane for different temperatures and density of $3 \cdot 10^{19}$ m^{-3}. The noise level corresponds to a SNR of about 16. At the edges of the measurable range, i.e. for 6 eV and 15.5 keV, there is a strong cross-correlation between density and temperature. Further from the margin of the measurable region, i.e. for 15 eV and 9.5 keV, the cross-correlation has to be considered in estimating the uncertainties. In the mid-temperature range illustrated with 110 eV, the posterior is close to Gaussian with very little or no cross-correlation. Asymmetric error bars can be important even without cross-correlation, as shown with 6.5 keV.

maximum. For example, points coloured green have a probability about e^{-4}–e^{-5} times less than in the maximum, which corresponds to the 3σ boundary of the normal distribution.

The Thomson posterior is found to depend on the value of the temperature, figure 8. For the values at the edges of the system design range there is a prevailing cross-correlation between temperature and density. For example for temperature of 6 eV, the posterior has a banana like shape, and for temperature of 15.5 keV the distribution has a cigar shape. The upper boundary in the latter case is determined by the prior. Since in both cases the regular way of specifying the maximum and the uncertainties may turn out to be problematic, they are considered here as being outside of the operational range. Nevertheless, such measurements can be useful if combined with other diagnostics. For temperatures away from the boundaries, temperatures of 15 eV and 9.5 keV in the figure, the distributions are more confined, but a significant T_e-n_e cross-correlation is still present and should be taken into account. In the middle of the temperature range, temperature of 110 eV in the figure, the distribution is very close to Gaussian without cross-correlation. In some cases, temperature of 6.5 keV in the figure, the distribution deviates considerably from Gaussian, but still has no cross-correlation. In such a case asymmetric uncertainties have to be specified.

The shape of posterior distribution also depends on the signal to noise ratio. In particular, asymmetric distributions without cross-correlation such as the one illustrated by a temperature of 6.5 keV are not pronounced for large SNR values. Instead, the distribution becomes Gaussian. Similarly, cases with asymmetric cross-correlated distributions such as the 15 eV and 9.5 keV distributions

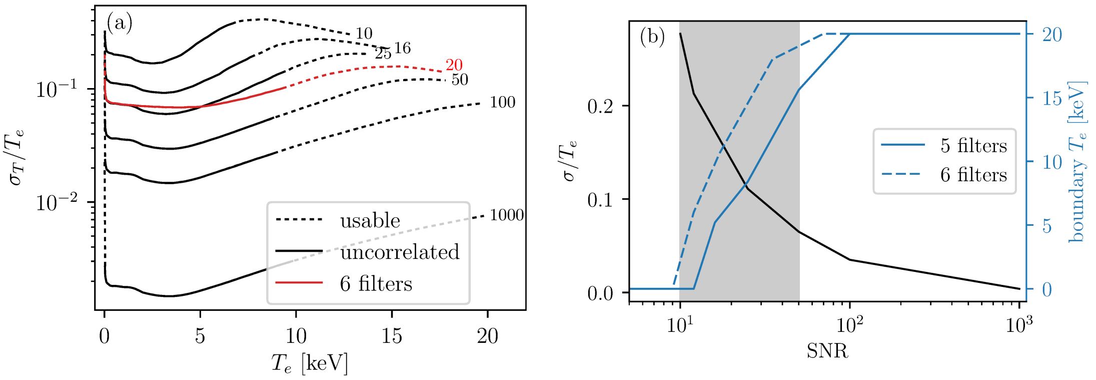

Figure 9. Scaling of errors with electron temperature and signal to noise ratio (SNR). (a) - dependence of the temperature uncertainty on the temperature for several SNR values. The black curves are for the standard W7-X polychromator with five spectral filters. The red curve is for a proposed 6-filter polychromator. (b) - dependence of the temperature and density uncertanties averaged over the measurable temperature range on the SNR value. Also, the boundary of the 12% uncertainty interval is shown for the 5 and 6 filter setups. The gray area indicates the SNR range obsrved in the first W7-X campaign.

in figure 8 become very close to Gaussian with modest cross-correlation, if SNR is high enough.

Results of the modelling are summarized in figure 9 in terms of uncertainties. The effective temperature uncertainty is plotted in figure 9a versus temperature for several SNR values. The uncertainty is defined here as width of the 95% confidence interval divided by four, which corresponds to $1 \cdot \sigma$ interval of normal distribution. The applied definition covers all densities and thus implicitly includes the cross-correlation. No further correction for the cross-correlation is required. The asymmetry of the confidence interval is not considered here. The dashed lines in figure 9 cover the range where reliable measurements are possible. Their ends correspond to the banana and cigar shaped posterior from the discussion above. The solid lines show the range with negligible cross-correlation between temperature and density. The SNR values are given for each line, the values being estimated from the maximal signal in all spectral channels. For the case of a very large SNR, the W7-X Thomson system is able to measure temperatures and densities without cross-correlation between about 10 eV and 10 keV. The value of the uncertainty varies with temperature and has a minimum between 1 keV and 5 keV. After the minimum, the uncertainty increases with the temperature. The roll-over visible for the low SNR cases is caused by the prior limit. For low SNR values, the measurement range becomes narrower.

Scaling of the average temperature and density uncertainties with signal to noise ratio is shown in figure 9b. The values are averaged over the whole usable range of temperatures including cases with the cross-correlation. For example, to achieve a relative temperature error of 10% the SNR must be around 30, and for 5% error, about 70. The SNR range covered in the first experimental campaign of W7-X is indicated with shaded area in the figure for comparison. The density uncertainty is about half that of the temperature, consistent with the fact that the density is determined by the total signal in all five channels.

The upper temperature boundary at which the uncertainty exceeds 12% is also presented in figure 9b. For high SNR values, reliable measurements are possible up to the end of the computation domain used here (20 keV). Reliable temperature measurements are not possible for SNR values less than about 10.

It was realized in the first W7-X campaign that measurements of electron temperatures of 10 keV and above are important. The W7-X Thomson performance degrades for such temperatures, especially if SNR is poor. To improve the Thomson performance at such temperatures a sixth spectral channel will be added to the polychromators that view the core plasma. In this new configuration, the present channels at 750–920 nm and 920–1000 nm will be split into three channels: 730–850 nm, 850–940 nm and 940–1000 nm. This modification can be readily accomplished, because the polychromator chassis is designed for six channels. The anticipated reduction in the uncertainties with the proposed 6 channel setup is illustrated in figure 9. The sixth channel indeed reduces the uncertainty for temperatures above about 5 keV and extends the measurement range.

6 Thomson scattering measurements in OP1.1

The W7-X limiter campaign, OP1.1, lasted 10 weeks: from December 2015 until March 2016. Plasma heating was provided by a 140 GHz electron cyclotron heating (ECRH) system with up to 4 MW of power. Because large parts of the first wall were note completed (unprotected CuCrZr surfaces) and because of the uncooled limiters, the total injected energy was limited to 4 MJ. This corresponds to 1 s long discharges at full power and to up to 6 s long discharges at reduced power. Only feed forward density control was available and the achievable stationary electron density was about $3 \cdot 10^{19}$ m^{-3} due to a limited wall conditioning and available heating power. For such low densities, the electron temperature up to 7 keV strongly exceeds the ion temperature up to 2 keV. The plasma is in the central electron root regime with positive radial electric field in the core [7, 8]. The overall plasma performance improved towards the end of the campaign as a result of improving wall conditions.

The Thomson scattering diagnostic operated reliably, with very few exceptions, from the very first W7-X discharges. A typical time resolved scattered light pulse together with the applied fitting can be found in figure 5b. The integrals of the fitted pulses are used to reconstruct the electron temperature and density using the Bayesian model. Evolution of the fitted integral is illustrated in figure 10a for a 6 s long experiment having a 4 s long plateau with ECRH heating of about 0.6 MW. The data are from the first spectral channel, 750–920 nm, from five selected scattering volumes. The error bars show the corresponding fit uncertainties. The electron temperatures reconstructed using all five spectral channels for the same discharge and for the same volumes are given in figure 10b. Both for the fit integral and for the calculated electron temperature and density, the modelled uncertainties are consistent with the standard deviations in flat top phases within about 30%. To achieve this, parameters of the avalanche photodiodes, like amplification and bandwidth, were adjusted to match signal variation in Raman calibration. An independent calibration of these photodiode parameters is still to be developed.

Bayesian analysis can be used to detect large scale systematic problems or inconsistencies in the data. Figure 10c shows the predictive posterior distribution of the signals in five spectral channels for a central scattering volume together with the measured data. The predictive posterior distribution is sampled with the Markov-Chain-Monte-Carlo procedure around the most probable values for the given experimental data and their uncertainties. Since the measured data are typically well

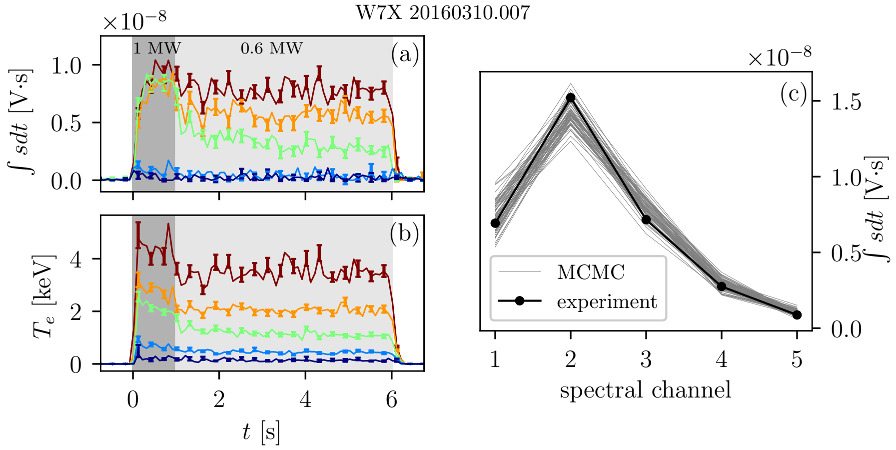

Figure 10. (a) - integrated scattered pulse signals from the first spectral channel (750–920 nm) for scattering volumes 4 (center), 6, 8, 10 and 12 (edge). This example is for a 6 s long discharge with heating power of 1 MW before 1 s and 0.6 MW afterwards. The error bars show the 1σ range. (b) - electron temperature for the same scattering volumes. (c) - predictive posterior distribution for five spectral channels. This example is for scattering volume 4 at about 2.4 s. The black curve represents the measured values, and the gray curves are possible realizations sampled with Markov-Chain-Monte-Carlo procedure.

covered with predictive posterior and no clear outliers are observed, the validity of the model and of the calibration is supported. Smaller scale problems in the calibration, such as those discussed below, are not easily indicated with this method and require more careful treatment.

For discharges with the ECRH resonance on the magnetic axis, the electron temperature is centrally peaked. Temperature profiles measured with the Thomson scattering diagnostic and with an electron cyclotron emission (ECE) diagnostic [38] are compared for the plateau phases of two discharges in figure 11. The ECE data include both sides of the profile, the low field side (LFS) and the high field side (HFS), averaged over the indicated time intervals. The shaded areas represent uncertainties of the ECE calibration, which is performed with a microwave source at liquid nitrogen and room temperatures. The Thomson scattering data are shown for every laser pulse with thin lines and as an average over the time intervals with symbols and heavier lines. The mapping of vacuum flux surfaces is used to superimpose data of both diagnostics.

The Thomson scattering measurements are in a good agreement with the ECE diagnostic in discharges with relatively low temperature and plasma pressure, figure 11a. In such cases both sides of the ECE profile also match. For higher temperatures and pressures the Thomson and ECE data are comparable, but some differences are observed, figure 11b. The two sides of the ECE measurements depart from each other, thus indicating a need for a full finite pressure equilibrium reconstruction. The Thomson measurements are about 20% lower in the center, and lie between the LFS and HFS branches of the ECE measurements at about mid-radius. In this rather low density plasmas with small optical depth, the central ECE radiation temperatures on the low field side tend to be increased due to the shine-through from the ECRH-heated core region.

The Thomson scattering results in figure 11b show a remaining calibration issue for the channels with Ge-doped fibers: scattering volumes 3 and 5. Because the Ge-doped fibers have a larger

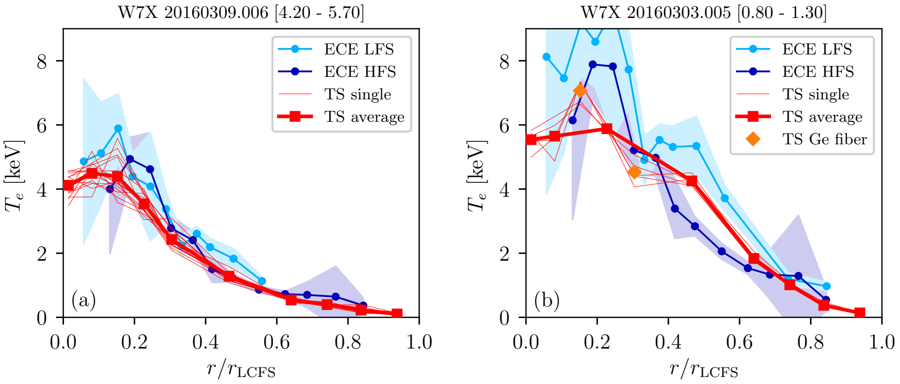

Figure 11. Comparison of electron temperature profiles measured with the Thomson scattering and electron cyclotron emission (ECE) diagnostics. The ECE diagnostic covers both sides of the profile. The shaded areas show calibration uncertainties of the ECE calibration. (a) - 6 s discharge with ECRH power of about 0.6 MW, central electron density of about $1 \cdot 10^{19}$ m^{-3}, central and volume averaged β of about 0.25% and 0.13% respectively. (b) - discharge with ECRH power of about 3.8 MW, central electron density of about $2.1 \cdot 10^{19}$ m^{-3}, central and volume averaged β of about 0.8% and 0.5% respectively. In this case, the average Thomson profile does not include Ge-fiber points because of the remaining calibration issues discussed in the text.

numerical aperture, they are more sensitive to the illumination conditions during the spectral calibration. In addition, a small calibration error is suspected for volume 1 due to possible shadowing by the in-vessel components. In order to improve the data consistency, calibration procedures will be further investigated and a suitable equilibrium reconstruction will be used in future experiments.
Electron density profiles are typically flat in the center with a gradient region in the outer half for discharges with on-axis ECRH heating. Three density profiles measured with the Thomson scattering system are presented in figure 12a for a discharge where the density was raised in three steps. Each profile is averaged over 2 to 4 laser pulses in the indicated time intervals. The error bars show the statistical 3σ intervals. The profiles are of similar shape, but have different amplitudes. In the central part of the profiles remaining systematic errors of the order of 5% are prominent. These errors are likely caused by the imperfect spectral calibration. The value of the error is consistent with the estimation from the Raman calibration in two spectral channels. It is worth noting that the shape of electron density profile can be affected by applying off-axis ECRH heating [8].
Electron densities measured with Thomson scattering can be validated against a single channel dispersion interferometer [39]. The laser path of the interferometer nearly coincides with that of the Thomson scattering system. Therefore, once the full profiles are available from the Thomson system, the comparison can be done without further assumptions by line integrating the Thomson data. In the first campaign only the outer half of the cross-section was covered, and as a consequence the values were mapped to the flux surfaces and afterwards integrated along the interferometer chord.

Thomson data integrated along the interferometer line are compared in figure 12b with the interferometer data for the same discharge as the one used to illustrate the profiles. Statistics of the ratio of the line integrated density from the two diagnostics is summarized in figure 12c for about 1200 Thomson laser pulses, which includes almost all measurements in the last three weeks of

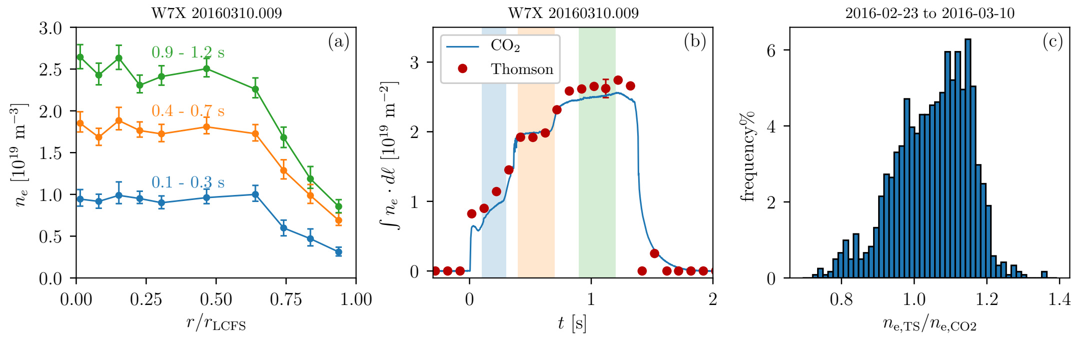

Figure 12. Profiles of electron density measured with Thomson scattering and comparison with a single channel interferometer. (a) - density profiles for three time intervals for a discharge, where the density was increased in three steps. This discharge was performed with on-axis ECRH heating. The error bars indicate the 3σ measurement uncertainties and do not include calibration uncertainties. (b) - line integrated density measured with the CO_2 interferometer and calculated from the Thomson scattering data. (c) - statistics of the ratio of the line integrated density from the Thomson data and from the interferometer. In total about 1200 measurement points are included.

the campaign (with exception of a very few discharges with a suspected misbehaviour of either Thomson or interferometer laser). In general, the Thomson scattering diagnostic overestimates the density by about 10% with respect to the interferometer.

The ratio of the density measured with the Thomson scattering and the interferometer is observed to change slightly between experimental days. These changes can not be explained by the systematic uncertainty of the Raman calibration of about 5%, but are more likely caused by changes in the Thomson laser adjustment. The adjustment can be affected between experimental days because the optics support structure is accessible and is used as a walkway to the central part of W7-X. For this reason an automated laser position control is presently under development.

The Thomson scattering diagnostic operated reliably throughout the first campaign and delivered temperatures compatible with the ECE measurements and densities in a reasonable agreement with the interferometer. The Thomson data are also used to estimate the plasma thermal energy, where the electron contribution dominates, and which is found to agree with the diamagnetic energy within about 25% [40]. One possible reason for the difference between the energies is the insufficiently diagnosed impurity content. Further discussion of this comparison can be found in the reference. The experimental Thomson data also show remaining systematic errors, in particular in the spectral calibration of the channels with Ge-doped fibers and in the density calibration. These questions will be addressed in future experiments by improving the calibration procedures and by implementing an improved laser alignment system.

7 Summary

The W7-X incoherent Thomson scattering diagnostic is an essential tool for the W7-X physics program because of its good spatial resolution, reliability and coverage of the full density range of 10^{19}–$2 \cdot 10^{20}$ m^{-3}. The exploration of the high density regime is an indispensable part of the experimental program, since the neoclassical transport scales favourably with the density and the disruptive density limit is absent in stellarators.

The W7-X Thomson system is a Nd:YAG setup with up to five lasers, each with pulse energy up to 2.4 J and repetition rate of 10 Hz. The laser light is guided through the plasma roughly horizontally and close to the magnetic axis. Two sets of lenses observe the entire plasma cross-section. The laser mirrors and the optics sets are mechanically decoupled from the machine for optical stability. The scattered light is transferred via fiber bundles to filter based polychromators. Presently, five spectral channels are used to cover the electron temperatures from 10 eV to 10 keV.

The relative spectral calibration of the system is carried out using a pulsed supercontinuum light source and a scanning monochromator. The light is delivered to a diffuse screen in front of the collection optics, and in such a way the full Thomson system with the exception of the vacuum window is calibrated simultaneously. However, the angular distribution of the light during the calibration is not equivalent to that in scattering experiments, which results in small systematic errors in plasma parameters.

The absolute calibration of the system is performed by observing anti-Stokes rotational Raman scattering in nitrogen in two spectral channels. The statistical uncertainty of this measurements is better than 1%. However, the results from the two spectral channels do show a larger difference for some volumes. This is likely caused by imperfections of the spectral calibration; the corresponding error is estimated to be about 4%. In addition, there is a uniform systematic uncertainty of 5% due to the molecular data.

The electron temperatures and densities are recovered by Bayesian modelling with the Minerva framework [23]. To test the Bayesian model and to verify the system performance simulations with synthetic data were used. Different types of the posterior distribution are found for different values of the signal to noise ratio and different temperature ranges. Close to Gaussian posterior distributions are observed in the middle of the design range, with asymmetric distributions arising on the edges of this range.

In the first campaign, OP1.1, the Thomson scattering diagnostic operated with one Nd:YAG laser and 10 scattering volumes. The temperature profiles measured with the Thomson scattering diagnostic are in a good agreement with an ECE diagnostic in discharges with relatively low temperature and pressure. Differences between the low and high field sides of the ECE measurements and the Thomson scattering are observed for higher temperatures and pressures. In order to improve the consistency, the calibration procedures will be further refined and a suitable equilibrium reconstruction will be used in future.

The electron density profiles measured with the Thomson scattering system indicate systematic errors between channels of the order of 5%, which is likely due to imperfections of the spectral calibration. The absolute values of the density are in a reasonable agreement with a single channel dispersion interferometer. The Thomson scattering diagnostic overestimates the line integrated density by about 10% with respect to the interferometer. This discrepancy is observed to vary between experimental days, as could be caused by changes in the laser adjustment because of an open access to the support structures. For this reason an automated laser position control is presently under development.

The W7-X Thomson scattering system will be extended for future experiments. Three lasers will be taken into operation, which will allow either a higher repetition rate up to 30 Hz, a higher pulse energy up to 6 J at 10 Hz, or a pulse train operation with 12 pulses each 100 μs with repetition rate of 5 Hz. The spatial resolution will be improved with up to 95 volumes in total and both sides of the profile will be covered. To improve the Thomson performance at temperatures above 10 keV it is foreseen to add a sixth spectral channel. For temperatures above 15 keV, dual wavelength measurements with the second laser at 1.3 μm are planned. To improve the spectral calibration, a new scheme employing Rayleigh scattering of light from a laser pumped OPO with a tunable wavelength is under development. This approach will remove the uncertainty due to the illumination conditions and will include the vacuum window and the deposited layers into the calibration.

Acknowledgments

The authors would like to thank Dr. R. Yasuhara for useful discussions and Dr. O. Ford for help with the Minerva framework.

This work has been carried out within the framework of the EUROfusion Consortium and has received funding from the Euratom research and training programme 2014-2018 under grant agreement No 633053. The views and opinions expressed herein do not necessarily reflect those of the European Commission.

References

[1] G. Grieger, C. Beidler, E. Harmeyer, J. Junker, J. Kißlinger, W. Lotz et al., Physics studies for helical-axis advanced stellarators, in Plasma Physics and Controlled Nuclear Fusion Research, Proceedings of the 12th International Conference, Nice, 1988, vol. 2, pp. 369 – 387, IAEA, Vienna, 1989.

[2] C. Beidler, G. Grieger, F. Herrnegger, E. Harmeyer, J. Kißlinger, W. Lotz et al., Physics and engineering design for Wendelstein VII-X, Fusion Technology **17** (1990) 148–168.

[3] R. C. Wolf, C. D. Beidler, A. Dinklage, P. Helander, H. P. Laqua, F. Schauer et al., Wendelstein 7-X program – demonstration of a stellarator option for fusion energy, IEEE Transactions on Plasma Science **44** (Sept, 2016) 1466–1471.

[4] G. Grieger, W. Lotz, P. Merkel, J. Nührenberg, J. Sapper, E. Strumberger et al., Physics optimization of stellarators, Physics of Fluids B: Plasma Physics **4** (1992) 2081–2091.

[5] J. Nührenberg, Development of quasi-isodynamic stellarators, Plasma Physics and Controlled Fusion **52** (2010) 124003.

[6] T. S. Pedersen, T. Andreeva, H.-S. Bosch, S. Bozhenkov, F. Effenberg, M. Endler et al., Plans for the first plasma operation of Wendelstein 7-X, Nuclear Fusion **55** (2015) 126001.

[7] T. Klinger, A. Alonso, S. Bozhenkov, R. Burhenn, A. Dinklage, G. Fuchert et al., Performance and properties of the first plasmas of Wendelstein 7-X, Plasma Physics and Controlled Fusion **59** (2017) 014018.

[8] R. C. Wolf et al., Major results from the first plasma campaign of the Wendelstein 7-X stellarator, accepted to Nuclear Fusion (2017) .

[9] J. Kißlinger, C. D. Beidler, E. Harmeyer, F. Rau, H. Renner and H. Wobig, Island divertor for the stellarator Wendelstein 7-X, in Controlled Fusion and Plasma Physisc, Proceedings of 21st European Conference, Montpellier, 1994, vol. 18B, part 1, pp. 368 – 371, European Physical Society, Geneva, 1994.

[10] H. Greuner, W. Bitter, F. Kerl, J. Kißlinger and H. Renner, Structure of divertor for the optimized stellarator W7-X, in Fusion Technology, Proceedings of 18th Symposium Karlsruhe, 1994, vol. 1, pp. 323 – 326, Elsevier, Amsterdam and New-York, 1995.

[11] H. Renner, J. Boscary, V. Erckmann, H. Greuner, H. Grote, J. Sapper et al., The capabilities of steady state operation at the stellarator W7-X with emphasis on divertor design, Nuclear Fusion **40** (2000) 1083 – 1093.

[12] G. Fuchert, S. Bozhenkov, M. Beurskens, A. Dinklage, Y. Feng, J. Geiger et al., Global energy confinement in the first operational phase of Wendelstein 7-X, PO4.00001, in 58th Annual Meeting of the APS Division of Plasma Physics; October 31–November 4 2016; San Jose, California, 2016.

[13] Matthias Hirsch et al., Confinement in Wendelstein 7-X limiter plasmas, accepted to Nuclear Fusion (2017) .

[14] I. Hutchinson, Principles of Plasma Diagnostics. Cambridge University Press, 2005.

[15] R. Pasqualotto, P. Nielsen, C. Gowers, M. Beurskens, M. Kempenaars, T. Carlstrom et al., High resolution Thomson scattering for Joint European Torus (JET), Review of Scientific Instruments **75** (2004) 3891–3893, [`http://dx.doi.org/10.1063/1.1787922`].

[16] B. Kurzan and H. D. Murmann, Edge and core Thomson scattering systems and their calibration on the ASDEX Upgrade tokamak, Review of Scientific Instruments **82** (2011) 103501, [`http://dx.doi.org/10.1063/1.3643771`].

[17] I. Yamada, K. Narihara, H. Funaba, R. Yasuhara, T. Kohmoto, H. Hayashi et al., Current status of the LHD Thomson scattering system, Journal of Instrumentation **7** (2012) C05007.

[18] T. N. Carlstrom, G. L. Campbell, J. C. DeBoo, R. Evanko, J. Evans, C. M. Greenfield et al., Design and operation of the multipulse Thomson scattering diagnostic on DIII-D (invited), Review of Scientific Instruments **63** (1992) 4901–4906, [`http://dx.doi.org/10.1063/1.1143545`].

[19] J. W. Hughes, D. Mossessian, K. Zhurovich, M. DeMaria, K. Jensen and A. Hubbard, Thomson scattering upgrades on Alcator C-Mod, Review of Scientific Instruments **74** (2003) 1667–1670, [`http://dx.doi.org/10.1063/1.1532764`].

[20] O. Naito, H. Yoshida and T. Matoba, Analytic formula for fully relativistic Thomson scattering spectrum, Physics of Fluids B **5** (1993) 4256–4258.

[21] O. Naito, H. Yoshida and T. Matoba, Erratum: "Analytic formula for fully relativistic Thomson scattering spectrum", Physics of Plasmas **1** (1994) 806.

[22] E. Pasch, M. N. A. Beurskens, S. A. Bozhenkov, G. Fuchert, J. Knauer and R. C. Wolf, The Thomson scattering system at Wendelstein 7-X, Review of Scientific Instruments **87** (2016) 11E729, [`http://aip.scitation.org/doi/pdf/10.1063/1.4962248`].

[23] J. Svensson and A. Werner, Large scale Bayesian data analysis for nuclear fusion experiments, in 2007 IEEE International Symposium on Intelligent Signal Processing, pp. 1–6, Oct, 2007. DOI.

[24] J. Cantarini, J. P. Knauer and E. Pasch, Design and study of the observation optics for the Thomson scattering planned at Wendelstein 7-X, AIP Conference Proceedings **993** (2008) 191–194, [`http://aip.scitation.org/doi/pdf/10.1063/1.2909106`].

[25] S. Hirshman, W. van RIJ and P. Merkel, Three-dimensional free boundary calculations using a spectral green's function method, Computer Physics Communications **43** (1986) 143 – 155.

[26] S. Schmuck, A. Dinklage, R. Fischer, J. P. Knauer, B. Kurzan, H.-D. Murmann et al., Design and calibration of a polychromator for the Thomson scattering at Wendelstein 7-X, AIP Conference Proceedings **993** (2008) 195–198, [`http://aip.scitation.org/doi/pdf/10.1063/1.2909107`].

[27] J. Howard, B. W. James and W. I. B. Smith, Rotational Raman calibration of Thomson scattering, Journal of Physics D: Applied Physics **12** (1979) 1435.

[28] B. P. LeBlanc, Thomson scattering density calibration by Rayleigh and rotational Raman scattering on NSTX, Review of Scientific Instruments **79** (2008) .

[29] I. Yamada, K. Narihara, H. Hayashi and L. E. Group, Raman calibration of the LHD YAG Thomson scattering for electron-density measurements, Review of Scientific Instruments **74** (2003) 1675–1678.

[30] M. Penney, R. S. Peters and M. Lapp, Absolute rotational Raman cross sections for N_2 , O_2 , and CO_2, Journal of Optical Society of America **64** (1974) 712–716.

[31] H. Schrötter and H. Klöckner, Raman scattering cross sections in gases and liquids in Raman spectroscopy of gases and liquids. Topics in current physics. Springer-Verlag, 1979.

[32] J. Bendtsen, The rotational and rotation-vibrational Raman spectra of $^{14}N_2$, $^{14}N^{15}N$ and $^{15}N_2$, Journal of Raman Spectroscopy **2** (1974) 133–145.

[33] D. S. Sivia and J. Skilling, Data Analysis: A Bayesian Tutorial. Oxford science publications. Oxford University Press, 2006.

[34] R. Fischer, C. Wendland, A. Dinklage, S. Gori, V. Dose and the W7-AS team, Thomson scattering analysis with the Bayesian probability theory, Plasma Physics and Controlled Fusion **44** (2002) 1501.

[35] R. Fischer, A. Dinklage and E. Pasch, Bayesian modelling of fusion diagnostics, Plasma Physics and Controlled Fusion **45** (2003) 1095.

[36] S. Kwak, J. Svensson, S. Bozhenkov, J. Flanagan, M. Kempenaars and Y.-C. Ghim, Bayesian modelling of JET high resolution Thomson scattering system using the Minerva framework, TO7.00014, in 58th Annual Meeting of the APS Division of Plasma Physics, October 31–November 4 2016, San Jose, California, vol. 61, 2016.

[37] W. K. Hastings, Monte Carlo sampling methods using Markov chains and their applications., Biometrika **57** (1970) 97–109.

[38] M. Hirsch, R. Burhenn, T. Estrada, H.-J. Hartfuss, W. Kasparek, A. Krämer-Flecken et al., Microwave and interferometer diagnostics for Wendelstein 7-X, in 41st EPS Conf. on Plasma Physics, Berlin, Germany (2014), P1.069;, 2014.

[39] J. Knauer, P. Kornejew, H. Trimino Mora, M. Hirsch, A. Werner and R. Wolf, A new dispersion interferometer for the stellarator Wendelstein 7-X, in 43rd EPS Conf. on Plasma Physics, Leuven, Belgium (2016), P4.017;, 2016.

[40] G. Fuchert to be published .